Chemical Science

ROYAL SOCIETY OF CHEMISTRY

EDGE ARTICLE

View Article Online
View Journal | View Issue

Cite this: *Chem. Sci.*, 2024, **15**, 6916

All publication charges for this article have been paid for by the Royal Society of Chemistry

Received 10th December 2023
Accepted 4th April 2024

DOI: 10.1039/d3sc06636c

rsc.li/chemical-science

Obtaining giant Rashba–Dresselhaus spin splitting in two-dimensional chiral metal–organic frameworks†

Shanshan Liu,[a] Ke Xu,*[c] Xingxing Li,*[ab] Qunxiang Li[ab] and Jinlong Yang[ab]

Two-dimensional (2D) nonmagnetic semiconductors with large Rashba–Dresselhaus (R–D) spin splitting at valence or conduction bands are attractive for magnetic-field-free spintronic applications. However, so far, the number of 2D R–D inorganic semiconductors has been quite limited, and the factors that determine R–D spin splitting as well as rational design of giant spin splitting, remain unclear. For this purpose, by exploiting 2D chiral metal–organic frameworks (CMOFs) as a platform, we theoretically develop a three-step screening method to obtain a series of candidate 2D R–D semiconductors with valence band spin splitting up to 97.2 meV and corresponding R–D coupling constants up to 1.37 eV Å. Interestingly, the valence band spin texture is reversible by flipping the chirality of CMOFs. Furthermore, five keys for obtaining giant R–D spin splitting in 2D CMOFs are successfully identified: (i) chirality, (ii) large spin–orbit coupling, (iii) narrow band gap, (iv) valence and conduction bands having the same symmetry at the Γ point, and (v) strong ligand field.

Introduction

One of the primary goals in spintronics is to utilize the spin degree of freedom of electrons for data storage and information transmission.[1,2] One promising approach is using the so-called Rashba–Dresselhaus (R–D) spin–orbit coupling (SOC) effect, which relies on the spin–orbit interaction of carriers in an inversion-asymmetric environment.[3–11] Due to such a SOC effect, the spin and momentum are entangled together, forming a spin texture in the momentum space. It holds significant importance for generating, manipulating, and detecting spin currents.[12] The most notable feature of the R–D effect is its capacity to manipulate spin exclusively through electric fields, without the need for external magnetic fields or magnetic exchange interactions, enabling potential applications in spin field-effect transistors (SFETs).[13,14] Despite the great potential of the R–D effect, achieving giant spin splitting in 2D materials is limited to a few inorganic semiconductors.[15–29] Moreover, the underlying factors influencing spin splitting and the general method to achieve giant spin splitting remain to be explored.

Considering the limited structural diversity and tunability of inorganic materials, we turn our attention to 2D metal–organic frameworks (MOFs).[30] Compared with inorganic materials, the properties of 2D MOFs can be easily designed by adjusting the metal nodes, ligand linkers, or connection modes between them. For the occurrence of R–D spin splitting, one of the basic requirements is to break the spatial inversion symmetry. Here, the combined term, R–D spin splitting, refers to either Rashba or Dresselhaus spin splitting. In this aspect, 2D chiral metal–organic frameworks (CMOFs) with the absence of inversion and mirror symmetries, provide a natural platform.[31–35] Constructed from chiral molecules and metals, 2D CMOFs serve as an important subclass of the MOF family and have received extensive attention in recent years,[36–42] especially in asymmetric catalysis[43] and enantioselective[44,45] applications. However, whether and how notable R–D spin splitting can be achieved in 2D CMOFs and the correlation between chirality and the R–D effect are still unclear.

To solve the above issues, we choose octahedrally coordinated metals (Sr–Sn and Ba–Pb) and different substituted bipyridine ligands with axial chirality to form a family of 2D CMOFs. Through a three-step screening process based on first-principles calculations, more than 20 2D CMOFs with obvious R–D spin splitting at the valence band (VB) are obtained. Among

[a]*Key Laboratory of Precision and Intelligent Chemistry, University of Science and Technology of China, Hefei, Anhui 230026, China. E-mail: lixx@ustc.edu.cn*

[b]*Hefei National Research Center for Physical Sciences at the Microscale, University of Science and Technology of China, Hefei, Anhui 230026, China*

[c]*Hubei Key Laboratory of Low Dimensional Optoelectronic Materials and Devices, School of Physics and Electronic Engineering, Hubei University of Arts and Science, Xiangyang, 441053, China. E-mail: xuke@hbuas.edu.cn*

† Electronic supplementary information (ESI) available: Group theory analysis, a possible route for the experimental synthesis, phonon spectrum and AIMD simulations for OsH_2(bipyridine_CN), HSE06 + SOC band structure for OsH_2(bipyridine_CN), the energy barrier for the transition from *R*-chiral to *S*-chiral OsH_2(bipyridine_CN) and the structure and Rashba spin splitting for the metastable intermediate state, R–D band splitting and spin texture schematic diagram, all 2D CMOFs generated during three-step screening, character table for C_2 and D_4 point groups, proportion of heavy elements in the valence band, and effects of strong field ligands on R–D spin splitting. See DOI: https://doi.org/10.1039/D3SC06636C

them, five structures possess R–D energies (ΔE) greater than 80 meV at the Γ point in the VB and R–D coupling constants (α) exceeding 1.20 eV Å, which are comparable to those reported for 2D inorganic materials.[15,16] In particular, the α of the 2D CMOF structure OsH_2(bipyridine_CN) reaches 1.37 eV Å, with the ΔE being 97.2 meV. Furthermore, we find that the VB spin texture is reversible *via* chirality inversion of 2D CMOFs. Finally, through systematical analysis of the above CMOFs, five main factors affecting the spin splitting are revealed: in addition to (i) chirality and (ii) strength of SOC, the following three factors also play a crucial role, that is, (iii) the size of the band gap, (iv) the symmetry of the VB and conduction band (CB) at the Γ point, and (v) ligand field strength.

Results and discussion

2D CMOF screening workflow

To generate the R–D spin splitting, two basic conditions need to be satisfied: the systems (i) break the spatial inversion symmetry[3,4] and (ii) have large spin–orbit coupling.[46] In addition, it is also generally accepted that the system is not magnetic. To fulfill these conditions, we utilize two inorganic ligands (L1) coordinated with heavy metal atoms (M) as nodes and axially chiral ligands[47–49] (L2) as linkers to form 2D CMOFs in a tetragonal lattice (Fig. 1a). In this structure, the two L1 ligands are axially connected to M, while the L2 ligands form four coordination bonds with M equatorially. Such an arrangement results in the metal center with an octahedral coordination configuration (Fig. 1a). For metal atoms (M), those from the fifth period (Sr to Sn) and sixth period (Ba to Pb) are selected. For the axial inorganic ligands (L1), the options are –I, –Br, –Cl, –F, –CN, and –H. For equatorial organic ligands (L2), 4,4′-bipyridine derivatives with axial chirality are chosen, and the axial chirality of the L2 ligand varies by using different substituent groups for X and Y (Fig. 1a).[50,51] If the Y group is –H, the L2 ligand is represented as bipyridine_X, and if the Y group is changed, it is represented as bipyridine_X_Y. The 2D CMOFs are denoted by ML1(bipyridine_X_Y). By adjusting the three degrees of freedom (M, L1, and L2), the 2D CMOFs with giant R–D energy (ΔE) are screened out through the following three steps (Fig. 1b):

Step I. The axial ligand (L1) is chosen as the halogen atom Cl, and the equatorial ligand (L2) is chosen as *R*-chiral bipyridine_I (bipyridine_I=[4,4′-bipyridine]-3,3′-diiodo). Note that such an axially chiral ligand can be easily synthesized in experiments.[52] By changing the metal center M, we obtain 23 CMOFs with the *C*2 space group and screen out 10 non-magnetic semiconductors. When M is Sr, Ru, Cd, Os, Pt, or Pb, spin splitting occurs in either the valence band or the conduction band (see Table S1† for more details). Among them, the splitting for Os-based CMOFs is significantly larger than that of other metal-based CMOFs, *i.e.*, the ΔE of $OsCl_2$(bipyridine_I) is 3.2 meV.

Step II. By using Os as the metal center and *R*-chiral bipyridine_I as the L2 ligand, we adjust the ligands L1 to obtain a larger R–D energy. The obtained CMOFs with the *C*2 space group are summarized in Table S2.† The most favorable L1 ligand is found to be –H, with the ΔE of OsH_2(bipyridine_I) being as large as 43.5 meV.

Step III. Fixing the metal center to be Os and the L1 ligand to be –H, the L2 ligand is now changed. The obtained CMOFs with *P*1, *C*2 and *P*422 space groups are summarized in Table S3.† The results show that when the L2 ligand is bipyridine_CN, *i.e.*, [4,4′-bipyridine]-3,3′-dicarbonitrile as synthesized in the experiment,[52] a giant and the biggest ΔE (97.2 meV) is achieved in OsH_2(bipyridine_CN).

Obviously, the combination of optimal L1 (–H) and L2 (bipyridine_CN) ligands helps largely improve the ΔE for Os-based CMOFs from 3.2 to 97.2 meV. Such enhancement is expected to be also applicable to other metal-based CMOFs. For instance, when the metal center is 4d transition metal Ru, the ΔE of RuH_2(bipyridine_CN) is enhanced to be 14.8 meV, representing a 28-fold increase compared to that of $RuCl_2$(bipyridine_I) (see Table S4†).

Dynamic and thermal stability analysis

Taking the outstanding OsH_2(bipyridine_CN) as an example, the structural stability is examined by phonon spectroscopy and *ab initio* molecular dynamics (AIMD) simulations. As shown in Fig. S1,† no obvious imaginary frequency is observed from the phonon spectrum, indicating that OsH_2(bipyridine_CN) is dynamically stable. Although some extremely small imaginary frequencies (less than 0.78 cm^{-1}) exist near the Γ point, they are considered to be unphysical and caused by size and boundary effects,[53] and a similar phenomenon has also been observed in other reported MOFs.[54–56] In addition, during 9 ps AIMD simulation at 600 K (Fig. S2†), the total energy fluctuates near its equilibrium value without any sudden drops, and the lattice structure remains intact without undergoing any reconstruction, confirming the good thermal stability of the structure.

Electronic structure and chirality

Fig. 2b and c show the band structures of the *R*-chiral OsH_2(bipyridine_CN) calculated using PBE and PBE + SOC, respectively. When the SOC is not considered, OsH_2(bipyridine_CN) is a direct band gap semiconductor (0.84 eV) with the valence band maximum (VBM) and conduction band minimum (CBM) located at the M point. All bands are spin degenerate. After including the SOC effect, the band gap is reduced to 0.60 eV. Moreover, the spin degeneracy is lifted, and its VBM and CBM are changed to locate between Γ and M points (near the Γ point) (Fig. 2c). In particular, the valence band presents a typical Dresselhaus spin splitting. The spin texture in the *k*-space for the split upper and lower branches is plotted in Fig. 2d, respectively. Near the Γ point, the in-plane spin texture of the upper branch exhibits anti-vortex geometry, which indicates a typical Dresselhaus-type SOC.[57] Interestingly, the spin texture of the lower branch shows a reverse anti-vortex geometry. The PBE + SOC band structure is further confirmed by using HSE06 + SOC calculations (Fig. S3†), which qualitatively give the same results.

Fig. 2f and g show the band structures of the *S*-chiral OsH_2(bipyridine_CN) calculated with the PBE and PBE + SOC, respectively. The band gap of *S*-chirality is the same as that of *R*-chirality. However, the valence band spin texture is totally

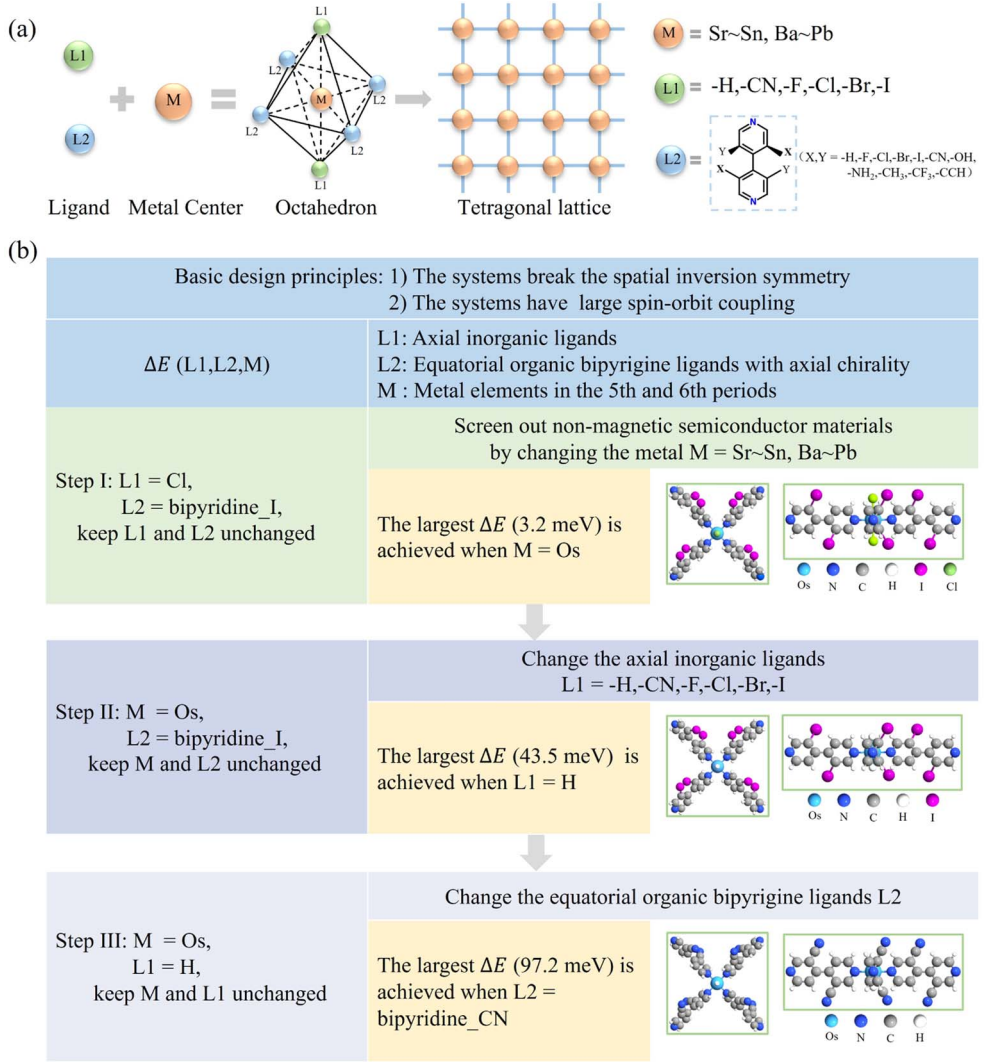

Fig. 1 (a) Structural composition diagram of 2D chiral metal–organic frameworks (CMOFs) in a tetragonal lattice. (b) The proposed three-step screening procedure to obtain 2D Rashba–Dresselhaus (R–D) semiconductors with large R–D spin splitting in CMOFs.

reversed compared to *R*-chirality (Fig. 2h). This indicates that the chirality inversion is a potential route to control the spin splitting. Experimentally, the chirality inversion could be realized using temperature, pressure, solvent, light, *etc.*[58–61] Here, a two-step transition path from *R*-chiral to *S*-chiral OsH_2(bipyridine_CN) is simulated (Fig. S4†), where the energy barrier is determined to be 0.7 eV. Such a big energy barrier allows the two enantiomers to coexist independently at room temperature. The space group of the metastable intermediate state is *Cm*, with the coexistence of *R*- and *S*-chiral bipyridine_CN ligands. Interestingly, the structure possesses a vortex Rashba-type spin texture, with the ΔE being 109 meV.

The effect of the band gap

To reveal the factors that affect the magnitude of spin splitting in 2D CMOFs, we plot ΔE *versus* band gap in Fig. 3a (see Tables S1–S3†). As shown in the upper-left corner of Fig. 3a, the systems OsH_2(bipyridine_CN), OsH_2(bipyridine_CCH), OsH_2(bipyridine_H), OsH_2(bipyridine_F) and OsH_2(bipyridine_OH) exhibit narrow band gaps and large R–D energies. The general trend is that the smaller the band gap, the bigger the spin splitting. However, there are several exceptions (marked by triangles), indicating that the band gap is not the only factor affecting spin splitting. For example, OsH_2(bipyridine_H) (0.52 eV) has a smaller band gap than OsH_2(bipyridine_CN) (0.6 eV), but its ΔE (88.5 meV) is smaller than that of OsH_2(bipyridine_CN) (97.2 meV). To explain this anomaly, factors other than the band gap need to be considered. Bahramy *et al.*[62] suggest that in the presence of a strong SOC, two states with the same symmetry can lead to a large spin splitting. In the next section, the effect of symmetry on the spin splitting will be investigated.

Fig. 3b shows the relationship between the ΔE and the α (see Tables S2 and S3† for more details). The R–D coupling constant is calculated using $\alpha = 2\Delta E/k_0$, where k_0 is the momentum-offset from the Γ point and ΔE is the R–D energy of spin splitting. In SFETs, a big α helps shorten the channel length,[63] which is

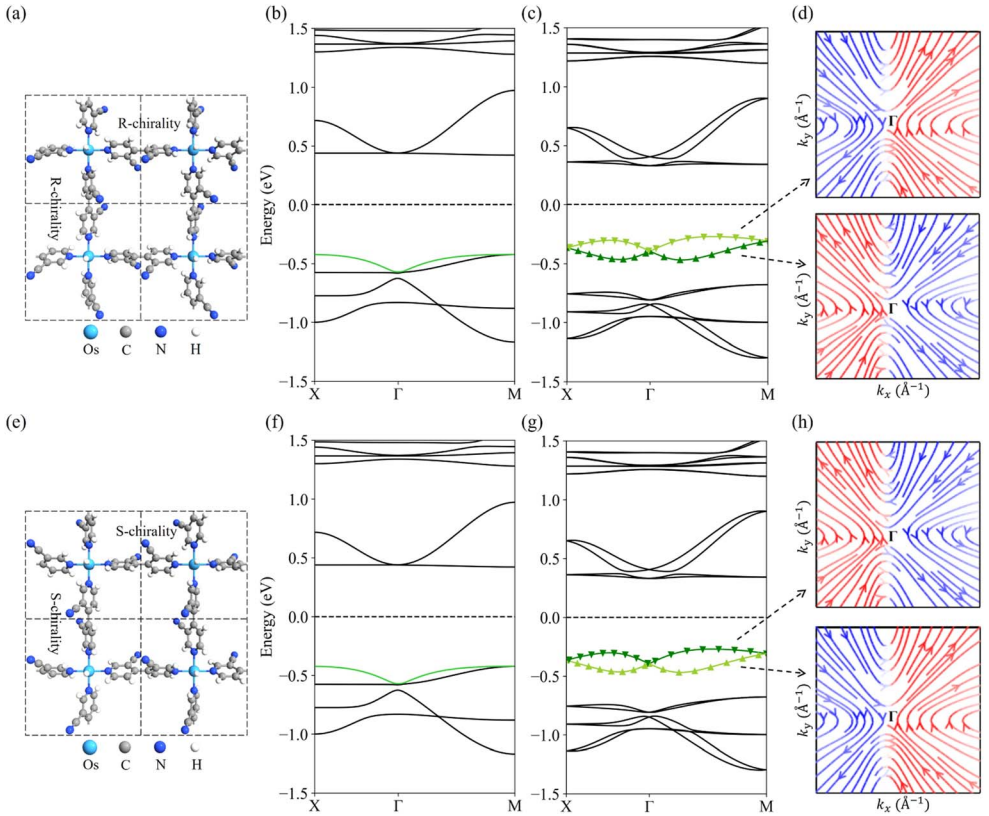

Fig. 2 (a) Structure of optimized *R*-chiral OsH_2(bipyridine_CN). Band structures calculated with (b) PBE and (c) PBE + SOC for *R*-chiral OsH_2(bipyridine_CN), and (d) its spin texture of upper and lower Dresselhaus bands in the valence band (VB). (e), (f), (g) and (h) are those for *S*-chiral OsH_2(bipyridine_CN). The tangent vectors of the streamlines (directions indicated by the arrows) in the spin texture represent the spin vector $\{s_x, s_y\}$ in the (k_x, k_y) plane, and the red (blue) color represents the positive (negative) spin component s_y. The Fermi levels are set to zero.

beneficial for maintaining spin coherence and improving integration of the spintronic devices. It is clear that the α is almost proportional to ΔE. When the ΔE is the largest (97.2 meV), the corresponding α reaches 1.37 eV Å. Therefore, to obtain a significant α, a large ΔE is needed.

The effect of symmetry

The symmetry characteristics of the VB and CB at the Γ point are determined by first-principles calculations combined with group-theory analysis. In the absence of SOC, for OsH_2(bipyridine_CN) with the $C2$ space group, all the bands at the Γ point are transformed according to the single-group representations of C_2. An important consideration is the presence of crystal field splitting (CFS), which affects the electronic structure of the system.[64] The projected band structure of OsH_2(bipyridine_CN) in Fig. 4a implies that the CB can be simply regarded as contributed by the p-orbital, while the VB is contributed by the d-orbital. The character table of the C_2 point

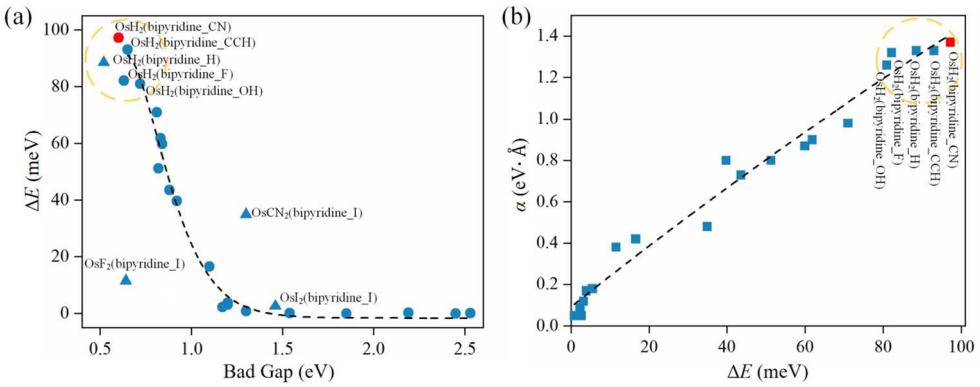

Fig. 3 (a) The relationship between the band gap and ΔE. (b) The relationship between ΔE and α.

group is shown in Table S5:† for the p-type CB, $\{p_z\} \rightarrow A$ and $\{p_x, p_y\} \rightarrow B$ and for the d-type VB, $\{d_{xy}, d_{z^2}\} \rightarrow A$ and $\{d_{yz}, d_{xz}\} \rightarrow B$. As shown in Fig. 4b, at the Γ point, the ordering of CFS for the VB and CB follows the sequence B → A and A → B, respectively, with increasing energy. When SOC is introduced, the previously defined single-group representation is transformed into a double-group representation. In the C_2 double point group, the reduction is $A \rightarrow \Gamma_3 \oplus \Gamma_4$ and $B \rightarrow \Gamma_3 \oplus \Gamma_4$ ($\Gamma_3 \oplus \Gamma_4$ is simplified as $\Gamma_{3,4}$). Fig. 4b shows that the VB and CB have the same symmetry $\Gamma_{3,4}$ at the Γ point. Furthermore, the SOC introduces a splitting between the $j = 3/2$ and $j = 1/2$ states of the p-level, and the $j = 5/2$ and $j = 3/2$ states of the d-level (a detailed discussion is in Note S1 of the ESI†).

For OsH_2(bipyridine_H), it belongs to the *P*422 space group and the Γ point has D_4 symmetry. Without SOC, all the bands at Γ are thus transformed according to the single-group representations of D_4. In Fig. 4c, the projected band structure of OsH_2(bipyridine_H) shows the dominant contributions of the d-orbital at the VB and the p-orbital at the CB. From the character table of the D_4 point group (Table S6†), it can be seen for the p-type CB that $\{p_x, p_y\} \rightarrow E$ and $\{p_z\} \rightarrow A_2$ and for the d-type VB, $\{d_{xy}\} \rightarrow B_2$, $\{d_{xz}, d_{yz}\} \rightarrow E$, $\{d_{z^2}\} \rightarrow A_1$ and $\{d_{x^2-y^2}\} \rightarrow B_1$. Fig. 4d gives the diagrammatic representation of band splitting caused by CFS and SOC. Without SOC, CFS for the VB (CB) at the Γ point follows the sequence E → B_2 (E → A_2), in an increasing order of energy. When SOC is incorporated, the previously defined single-group representation is transformed into a double-group representation. In the D_4 double point group, the reduction is $A_2 \rightarrow \Gamma_6$, $E \rightarrow \Gamma_6 \oplus \Gamma_7$, $B_2 \rightarrow \Gamma_7$, $A_1 \rightarrow \Gamma_6$ and $B_1 \rightarrow \Gamma_7$. In other words, B_1 and B_2 transform to Γ_7 and A_1 and A_2 transform to Γ_6, whereas E splits into two two-fold bands: Γ_6 and Γ_7. Obviously, the VB and CB at the Γ point exhibit different symmetries. Since two states with the same symmetry are beneficial for enhancing spin splitting,[62] OsH_2(bipyridine_CN), which has the same symmetry at the Γ point in the VB and CB, possesses a larger ΔE than OsH_2(bipyridine_H).

The effect of ligand field strength

According to ligand field theory,[65] the ligand field strength can be described by the spectrochemical series: –I < –Br < –Cl < –F <

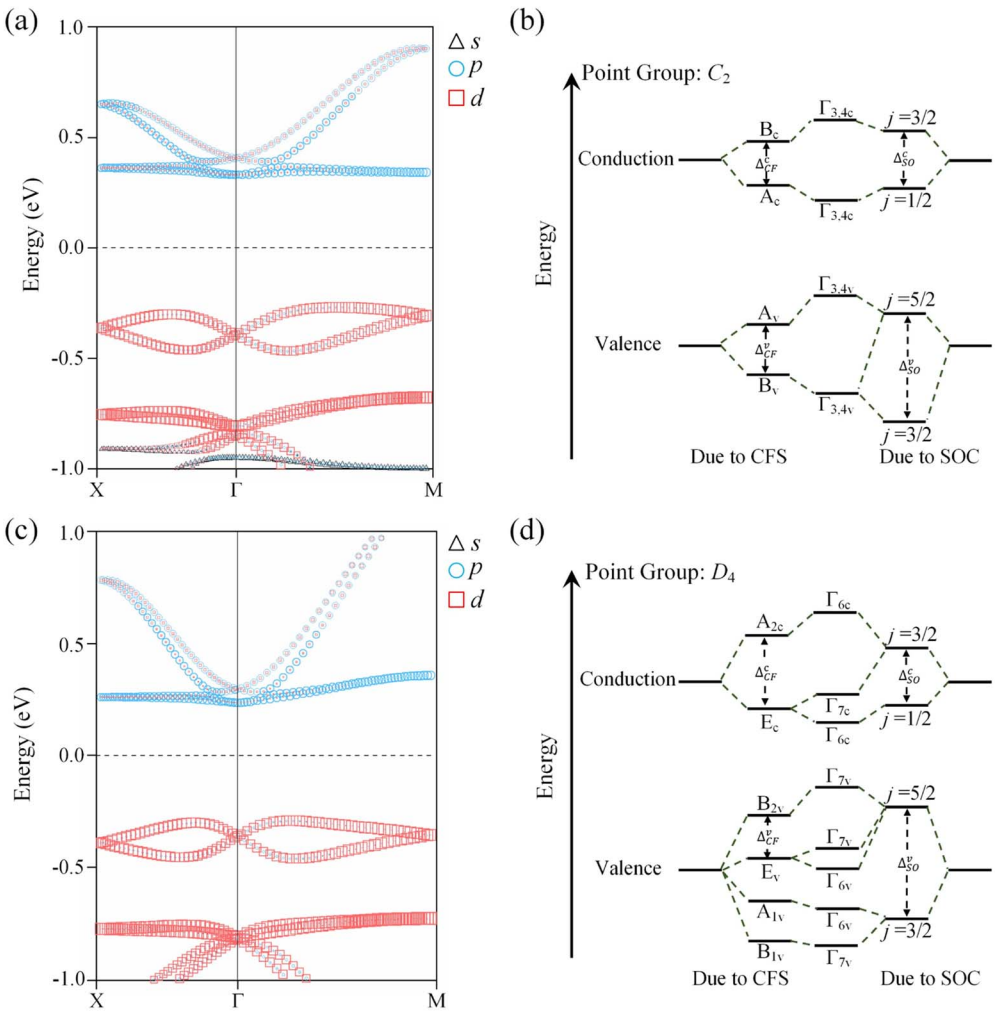

Fig. 4 Projected band structure of (a) OsH_2(bipyridine_CN) and (c) OsH_2(bipyridine_H). Illustration of the band splitting of (b) OsH_2(bipyridine_CN) and (d) OsH_2(bipyridine_H) due to a combination of crystal field splitting (CFS) and spin–orbit coupling (SOC), where ΔCF denotes the crystal field splitting energy and ΔSO denotes the atomic SOC energy.

–CN.[66,67] During the screening process, we find that the ligand field strength also has a notable influence on the spin splitting (see Table S2†). The ligand field strength indirectly affects the ΔE by varying the spin–orbit coupling. A stronger ligand field can increase the proportion of metal atoms in the VB, thereby inducing a more efficient SOC.[68] In Table S7†, the proportion of Os metal atoms in the VB increases with the increase of ligand field strength, which results in an enhancement in ΔE. According to the ligand field strength, the anomalies of $Os(CN)_2$(bipyridine_I), OsF_2(bipyridine_I) and OsI_2(-bipyridine_I) in Fig. 3a can be well explained. For OsF_2(-bipyridine_I) and $Os(CN)_2$(bipyridine_I), their VB and CB have the same symmetry at the Γ point, and the band gap of the former (0.64 eV) is smaller than that of the latter (1.30 eV). Without considering the influence of ligand field strength, the ΔE of OsF_2(bipyridine_I) is expected to be larger than that of $Os(CN)_2$(bipyridine_I). However, the stronger ligand field strength of –CN endows $Os(CN)_2$(bipyridine_I) (34.9 meV) with a larger ΔE than OsF_2(bipyridine_I) (11.5 meV). Additionally, we have tested other strong field ligands including NCS^-, NO_2^-, PH_3, and CO. The calculation results show that the energy of spin splitting increases as the ligand field strength increases (see Table S8†). Another factor worth noting is the SOC strength of the ligand itself. For OsI_2(bipyridine_I) and $OsBr_2$(-bipyridine_I), though the ligand field strength of –I is weaker than that of –Br, the ligand –I is heavier than –Br, resulting in a much stronger SOC of OsI_2(bipyridine_I). Consequently, OsI_2(bipyridine_I) has a larger ΔE than $OsBr_2$(bipyridine_I) (see Table S2†).

Finally, based on the above discussions, five conditions required for obtaining giant spin splitting in 2D CMOFs are identified: (i) the presence of chiral ligands, which breaks the inversion symmetry, (ii) the existence of heavy atoms, which leads to a significant spin–orbit coupling, (iii) a narrow band gap, (iv) the same symmetry of the VB and CB at the Γ point, and (v) the presence of strong field ligands.[69,70]

An important factor for designing spin field-effect transistors (SFETs) based on R–D semiconductors is the channel length $L = \pi\hbar^2/(2m^*\alpha)$,[63] over which the spin precesses by π (180°). To improve the integration, a short channel length is desired, which requires a large α. Taking the best OsH_2(bipyridine_CN) as an example, the calculated carrier effective mass m^* and coupling constant α of the valence band are 1.96 m_e and 1.37 eV Å, respectively. According to the formula $L = \pi\hbar^2/(2m^*\alpha)$, we find that to achieve a spin precession of 180°, the required channel length (L) is 0.45 nm. This value is challenging to attain with previous 2D semiconductors and is ideal for miniaturized nano-spintronic devices. Moreover, a possible synthesis route for OsH_2(bipyridine_CN) is proposed (more details can be found in Note S2 of the ESI†).

Conclusions

In summary, based on first-principles calculations, we report an unprecedented class of 2D CMOFs with significant R–D spin splitting. Among them, OsH_2(bipyridine_CN) demonstrates an R–D energy ΔE of 97.2 meV and a coupling constant A of 1.37 eV Å. Additionally, the underlying factors that control the R–D spin splitting have been revealed, which can lead to the future development of 2D R–D semiconductors with giant spin splitting.

Computational methods

Rashba spin–orbit coupling

The Rashba spin–orbit coupling term is induced by the structure inversion asymmetry. The effective Rashba Hamiltonian can be represented as:[71]

$$H_{\text{eff}} = \frac{\boldsymbol{p}^2}{2m^*} + \alpha_{\text{R}}(\boldsymbol{\sigma} \times \boldsymbol{k})\cdot\hat{z} \quad (1)$$

where $\boldsymbol{p}$ is the electron momentum, m^* is the electron effective mass, α_{R} is the coupling constant, $\boldsymbol{\sigma}$ is the Pauli matrix, $\boldsymbol{k}$ is the electron wave vector, and $\hat{z}$ is the unit normal vector. The corresponding eigenvalues are:

$$E_{\pm}(\boldsymbol{k}) = \frac{h^2k^2}{8\pi^2m^*} \pm \alpha_{\text{R}}k = \frac{h^2}{8\pi^2m^*}(k \pm k_0)^2 - \Delta\boldsymbol{E}_{\mathbf{R}} \quad (2)$$

where the symbol + (−) denotes the upper (lower) branch, ΔE_{R} is the energy difference between $k = k_0$ and $k = 0$, and k_0 is the momentum offset between the peak and the high symmetry point. Therefore, according to eqn (2) the Rashba coupling constant α_{R} can be simply calculated as:

$$\alpha_{\text{R}} = \frac{2\Delta\boldsymbol{E}_{\text{R}}}{k_0} \quad (3)$$

Dresselhaus spin–orbit coupling

The Dresselhaus spin–orbit coupling term arises from bulk inversion asymmetry. The 2D Dresselhaus Hamiltonian can be represented as:[72]

$$H_{\text{D}}(\boldsymbol{k}) = \alpha_{\text{D}}(k_x\sigma_x - k_y\sigma_y) \quad (4)$$

where the constant α_{D} is the Dresselhaus spin–orbit coupling strength. The eigenvalues are:

$$E_{\pm}(\boldsymbol{k}) = \frac{h^2k^2}{8\pi^2m^*} \pm \alpha_{\text{D}}k = \frac{h^2}{8\pi^2m^*}(k \pm k_0)^2 - \Delta E_{\text{D}} \quad (5)$$

where the symbol + (−) denotes the upper (lower) branch, ΔE_{D} is the energy difference between $k = k_0$ and $k = 0$, and k_0 is the momentum offset between the peak and the high symmetry point. The Dresselhaus coupling constant α_{D} can be simply calculated as:

$$\alpha_{\text{D}} = \frac{2\Delta E_{\text{D}}}{k_0} \quad (6)$$

For calculating the $\alpha_{\text{R/D}}$, we find k_0 and $\Delta E_{\text{R/D}}$ through the parabolic fitting of the energy band where spin splitting occurs and calculate the $\alpha_{\text{R/D}}$ through eqn (3) and (6). ΔE_{R} and ΔE_{D} are indistinguishable solely from the band structure (see Fig. S5a and b†) but can be distinguished through the spin texture. In general, the Rashba and Dresselhaus spin textures exhibit

vortex and antivortex geometries in the k_x–k_y plane (see Fig. S5c and d†).

The electronic structures of 2D CMOFs are calculated based on the density functional theory (DFT) method within the Perdew–Burke–Ernzerhof (PBE) generalized gradient approximation (GGA)[73] implemented in the Vienna *ab initio* simulation package (VASP).[74] A projector augmented wave (PAW) potential and a plane-wave cut-off energy of 500 eV are used. The vacuum space along the z direction is 15 Å. The first Brillouin zone is sampled with a Monkhorst–Pack grid of $3 \times 3 \times 1$. Both the lattice constant and the positions of all atoms are relaxed until the force is less than 0.01 eV Å^{-1}. The criterion for the total energy is set as 1×10^{-6} eV. In our calculations of all the materials, each transition metal atom is given a notable initial magnetic moment to find its optimal value. By checking the converged local magnetic moments, the magnetic properties of the material are identified, that is, if the local magnetic moment of each atom is zero, the material is determined to be non-magnetic, otherwise, it is magnetic. The HSE06 functional (ref. 75) is used to ensure the accuracy of the PBE results, and then all materials are screened using the PBE to save the computation time. The phonon spectrum is simulated by using the finite displacement method as implemented in the Phonopy package interfaced with the VASP.[76] A $3 \times 3 \times 1$ supercell with a Monkhorst–Pack k-point mesh of $1 \times 1 \times 1$ is adopted. The thermal stability is assessed according to AIMD simulations at 600 K by using a $2 \times 2 \times 1$ supercell. The band symmetry is calculated using the Quantum Espresso package.[77]

Author contributions

X. Li conceived the idea for this study and designed the experiments. S. Liu performed the calculations. K. Xu helped with the analysis and interpretation of the data. S. Liu wrote the manuscript and all authors assisted with editing, analysis, and interpretation.

Conflicts of interest

The authors declare no competing financial interest.

Acknowledgements

This work was supported by the National Natural Science Foundation of China (22288201, 22273092, 22322304, and 22373095), the Strategic Priority Research Program of the Chinese Academy of Sciences (XDB0450101), the Innovation Program for Quantum Science and Technology (2021ZD0303306), and USTC Tang Scholar.

References

1 X. L. Yan, X. Su, J. Chen, C. Jin and L. Chen, *Angew. Chem., Int. Ed.*, 2023, **62**, e202305408.
2 S. H. Yang, R. Naaman, Y. Paltiel and S. S. P. Parkin, *Int. Rev. Phys.*, 2021, **3**, 328–343.
3 E. I. Rashba, *Sov. Phys. Solid State*, 1960, **2**, 1109–1122.
4 G. Dresselhaus, *Phys. Rev.*, 1955, **100**, 580–586.
5 Y. Wang, C. C. Xiao, M. G. Chen, C. Q. Hu, J. D. Zou, C. Wu, J. Z. Jiang, S. Y. A. Yang, Y. H. Lu and W. Ji, *Mater. Horiz.*, 2018, **5**, 521–528.
6 H. Q. Ai, X. K. Ma, X. F. Shao, W. F. Li and M. W. Zhao, *Phys. Rev. Mater.*, 2019, **3**, 054407.
7 M. U. Farooq, L. D. Xian and L. Huang, *Phys. Rev. B*, 2022, **105**, 245405.
8 F. Nagasawa, A. A. Reynoso, J. P. Baltanas, D. Frustaglia, H. Saarikoski and J. Nitta, *Phys. Rev. B*, 2018, **98**, 245301.
9 C. E. Whittaker, T. Dowling, A. V. Nalitov, A. V. Yulin, B. Royall, E. Clarke, M. S. Skolnick, I. A. Shelykh and D. N. Krizhanovskii, *Nat. Photonics*, 2021, **15**, 193–196.
10 A. Stroppa, D. Di Sante, P. Barone, M. Bokdam, G. Kresse, C. Franchini, M. H. Whangbo and S. Picozzi, *Nat. Commun.*, 2014, **5**, 5900.
11 L. Meier, G. Salis, I. Shorubalko, E. Gini, S. Schön and K. Ensslin, *Nat. Phys.*, 2007, **3**, 650–654.
12 A. Soumyanarayanan, N. Reyren, A. Fert and C. Panagopoulos, *Nature*, 2016, **539**, 509–517.
13 J. Ingla-Aynes, F. Herling, J. Fabian, L. E. Hueso and F. Casanova, *Phys. Rev. Lett.*, 2021, **127**, 047202.
14 H. C. Koo, S. B. Kim, H. Kim, T. E. Park, J. W. Choi, K. W. Kim, G. Go, J. H. Oh, D. K. Lee, E. S. Park, I. S. Hong and K. J. Lee, *Adv. Mater.*, 2020, **32**, 2002117.
15 K. Wu, J. J. Chen, H. H. Ma, L. Y. Wan, W. Hu and J. L. Yang, *Nano Lett.*, 2021, **21**, 740–746.
16 J. J. Che, K. Wu, W. Hu and J. L. Yang, *J. Am. Chem. Soc.*, 2022, **144**, 20035–20046.
17 M. K. Jana, R. Y. Song, H. L. Liu, D. R. Khanal, S. M. Janke, R. D. Zhao, C. Liu, Z. V. Vardeny, V. Blum and D. B. Mitzi, *Nat. Commun.*, 2020, **11**, 4699.
18 X. M. Fu, C. Jia, L. Sheng, Q. X. Li, J. L. Yang and X. X. Li, *J. Phys. Chem. Lett.*, 2023, **14**, 11292–11297.
19 S. Singh and A. H. Romero, *Phys. Rev. B*, 2017, **95**, 165444.
20 T. Hu, F. H. Jia, G. D. Zhao, J. Y. Wu, A. Stroppa and W. Ren, *Phys. Rev. B*, 2018, **97**, 235404.
21 X. Y. Chin, D. Cortecchia, J. Yin, A. Bruno and C. Soci, *Nat. Commun.*, 2015, **6**, 7383.
22 A. B. Maghirang, R. A. B. Villaos, M. N. R. Perez, L. Y. Feng, Z. Q. Huang, C. H. Hsu and F. C. Chuang, *ACS Appl. Electron. Mater.*, 2022, **4**, 5308–5316.
23 J. F. Khoury, J. G. He, J. E. Pfluger, I. Hadar, M. Balasubramanian, C. C. Stoumpos, R. Zu, V. Gopalan, C. Wolverton and M. G. Kanatzidis, *Chem. Sci.*, 2020, **11**, 870–878.
24 A. B. Maghirang, G. Macam, A. L. Sufyan, Z. Q. Huang, C. H. Hsu and F. C. Chuang, *Chin. J. Phys.*, 2022, **77**, 2346–2354.
25 P. A. L. Sino, L. Y. Feng, R. A. B. Villaos, H. N. Cruzado, Z. Q. Huang, C. H. Hsu and F. C. Chuang, *Nanoscale Adv.*, 2021, **3**, 6608–6616.
26 B. Maurer, C. Vorwerk and C. Draxl, *Phys. Rev. B*, 2022, **105**, 8.
27 M. K. Jana, R. Y. Song, Y. Xie, R. D. Zhao, P. C. Sercel, V. Blum and D. B. Mitzi, *Nat. Commun.*, 2021, **12**, 4982.
28 M. Kepenekian, R. Robles, C. Katan, D. Sapori, L. Pedesseau and J. Even, *ACS Nano*, 2015, **9**, 11557–11567.

29 M. T. Pham, E. Amerling, T. A. Ngo, H. M. Luong, K. Hansen, H. T. Pham, T. N. Vu, H. Tran, L. Whittaker-Brooks and T. D. Nguyen, *Adv. Opt. Mater.*, 2022, **10**, 2101232.
30 H. Furukawa, K. E. Cordova, M. O'Keeffe and O. M. Yaghi, *Science*, 2013, **341**, 1230444.
31 L. D. Barron, *Chem. Soc. Rev.*, 1986, **15**, 189–223.
32 S. Weigelt, C. Busse, L. Petersen, E. Rauls, B. Hammer, K. V. Gothelf, F. Besenbacher and T. R. Linderoth, *Nat. Mater.*, 2006, **5**, 112–117.
33 J. Wencel-Delord, A. Panossian, F. R. Leroux and F. Colobert, *Chem. Soc. Rev.*, 2015, **44**, 3418–3430.
34 M. H. Liu, L. Zhang and T. Y. Wang, *Chem. Rev.*, 2015, **115**, 7304–7397.
35 Y. Yang, J. Liang, F. Pan, Z. Wang, J. Q. Zhang, K. Amin, J. Fang, W. J. Zou, Y. L. Chen, X. H. Shi and Z. X. Wei, *Nat. Commun.*, 2018, **9**, 3808.
36 W. Gong, Z. J. Chen, J. Q. Dong, Y. Liu and Y. Cui, *Chem. Rev.*, 2022, **122**, 9078–9144.
37 Q. S. Cheng, Q. Ma, H. B. Pei, H. Liang, X. J. Zhang, X. N. Jin, N. J. Liu, R. B. Guo and Z. L. Mo, *Coord. Chem. Rev.*, 2023, **484**, 215120.
38 Y. H. Liu, L. M. Liu, X. Chen, Y. Liu, Y. Han and Y. Cui, *J. Am. Chem. Soc.*, 2021, **143**, 3509–3518.
39 J. Guo, Y. Zhang, Y. F. Zhu, C. Long, M. T. Zhao, M. He, X. F. Zhang, J. W. Lv, B. Han and Z. Y. Tang, *Angew. Chem., Int. Ed.*, 2018, **57**, 6873–6877.
40 Z. Sharifzadeh, K. Berijani and A. Morsali, *Coord. Chem. Rev.*, 2021, **445**, 214083.
41 T. H. Zhao, J. L. Han, Y. H. Shi, J. Zhou and P. F. Duan, *Adv. Mater.*, 2021, **33**, 2101797.
42 L. A. Hall, D. M. D'Alessandro and G. Lakhwani, *Chem. Soc. Rev.*, 2023, **52**, 3567–3590.
43 H. Zhang, L. L. Lou, K. Yu and S. X. Liu, *Small*, 2021, **17**, 2005686.
44 Z. Z. Weng, H. Xu, W. Zhang, G. L. Zhuang, L. S. Long, X. J. Kong and L. S. Zheng, *ACS Appl. Mater. Interfaces*, 2021, **13**, 37402–37411.
45 J. P. Zhao, J. Luo, Z. H. Lin, X. Chen, G. H. Ning, J. Z. Liu and D. Li, *Inorg. Chem. Front.*, 2022, **9**, 4907–4912.
46 M. Nagano, A. Kodama, T. Shishidou and T. Oguchi, *J. Phys.: Condens. Matter*, 2009, **21**, 064239.
47 S. Y. Yan, W. Xia, S. Y. Li, Q. L. Song, S. H. Xiang and B. Tan, *J. Am. Chem. Soc.*, 2020, **142**, 7322–7327.
48 D. Zhang and Q. R. Wang, *Coord. Chem. Rev.*, 2015, **286**, 1–16.
49 M. McCarthy and P. J. Guiry, *Tetrahedron*, 2001, **57**, 3809–3844.
50 A. Rang, M. Engeser, N. M. Maier, M. Nieger, W. Lindner and C. A. Schalley, *Chem.–Eur. J.*, 2008, **14**, 3855–3859.
51 V. Mamane, E. Aubert, P. Peluso and S. Cossu, *J. Org. Chem.*, 2012, **77**, 2579–2583.
52 J. Richard, J. Joseph, C. Wang, A. Ciesielski, J. Weiss, P. Samori, V. Mamane and J. A. Wytko, *J. Org. Chem.*, 2021, **86**, 3356–3366.
53 J. L. Lu, G. Chen, W. Luo, J. Iñiguez, L. Bellaiche and H. J. Xiang, *Phys. Rev. Lett.*, 2019, **122**, 227601.
54 X. Y. Li, Q. B. Liu, Y. S. Tang, W. Li, N. Ding, Z. Liu, H. H. Fu, S. Dong, X. X. Li and J. L. Yang, *J. Am. Chem. Soc.*, 2023, **145**, 7869–7878.
55 H. F. Lv, X. Y. Li, D. X. Wu, Y. Liu, X. X. Li, X. J. Wu and J. L. Yang, *Nano Lett.*, 2022, **22**, 1573–1579.
56 C. Tang, L. Zhang, S. Sanvito and A. J. Du, *J. Am. Chem. Soc.*, 2023, **145**, 2485–2491.
57 C. M. Acosta, L. D. Yuan, G. M. Dalpian and A. Zunger, *Phys. Rev. B*, 2021, **104**, 104408.
58 J. B. Yao, W. H. Wu, W. T. Liang, Y. J. Feng, D. Y. Zhou, J. J. Chruma, G. Fukuhara, T. Mori, Y. Inoue and C. Yang, *Angew. Chem., Int. Ed.*, 2017, **56**, 6869–6873.
59 C. Xiao, W. H. Wu, W. T. Liang, D. Y. Zhou, K. Kanagaraj, G. Cheng, D. Su, Z. H. Zhong, J. J. Chruma and C. Yang, *Angew. Chem., Int. Ed.*, 2020, **59**, 8094–8098.
60 L. B. Wang, L. Yin, W. Zhang, X. L. Zhu and M. Fujiki, *J. Am. Chem. Soc.*, 2017, **139**, 13218–13226.
61 H. K. Bisoyi and Q. Li, *Angew. Chem., Int. Ed.*, 2016, **55**, 2994–3010.
62 M. S. Bahramy, R. Arita and N. Nagaosa, *Phys. Rev. B: Condens. Matter Mater. Phys.*, 2011, **84**, 041202.
63 S. Gupta and B. I. Yakobson, *J. Am. Chem. Soc.*, 2021, **143**, 3503–3508.
64 F. A. Cotton, *Chemical applications of group theory*, John Wiley & Sons, 1991.
65 J. Griffith and L. Orgel, *Q. Rev., Chem. Soc.*, 1957, **11**, 381–393.
66 J. Glerup, O. Monsted and C. E. Schaffer, *Inorg. Chem.*, 1976, **15**, 1399–1407.
67 L. Carlton, *Magn. Reson. Chem.*, 2004, **42**, 760–768.
68 Z. R. Hao, K. Zhang, K. Chen, P. Wang, Z. Y. Lu, W. G. Zhu and Y. Liu, *Dalton Trans.*, 2020, **49**, 8722–8733.
69 N. Kunkel, H. Kohlmann, A. Sayede and M. Springborg, *Inorg. Chem.*, 2011, **50**, 5873–5875.
70 S. Aldridge and A. J. Downs, *Chem. Rev.*, 2001, **101**, 3305–3366.
71 T. Etienne, E. Mosconi and F. De Angelis, *J. Phys. Chem. Lett.*, 2016, **7**, 1638–1645.
72 M. Studer, M. P. Walser, S. Baer, H. Rusterholz, S. Schon, D. Schuh, W. Wegscheider, K. Ensslin and G. Salis, *Phys. Rev. B: Condens. Matter Mater. Phys.*, 2010, **82**, 235320.
73 J. P. Perdew, K. Burke and M. Ernzerhof, *Phys. Rev. Lett.*, 1996, **77**, 3865–3868.
74 G. Kresse and J. Furthmuller, *Phys. Rev. B: Solid State*, 1996, **54**, 11169–11186.
75 J. Heyd, G. E. Scuseria and M. Ernzerhof, *J. Chem. Phys.*, 2006, **124**, 219906.
76 K. Parlinski, Z. Q. Li and Y. Kawazoe, *Phys. Rev. Lett.*, 1997, **78**, 4063–4066.
77 P. Giannozzi, S. Baroni, N. Bonini, M. Calandra, R. Car, C. Cavazzoni, D. Ceresoli, G. L. Chiarotti, M. Cococcioni, I. Dabo, A. Dal Corso, S. de Gironcoli, S. Fabris, G. Fratesi, R. Gebauer, U. Gerstmann, C. Gougoussis, A. Kokalj, M. Lazzeri, L. Martin-Samos, N. Marzari, F. Mauri, R. Mazzarello, S. Paolini, A. Pasquarello, L. Paulatto, C. Sbraccia, S. Scandolo, G. Sclauzero, A. P. Seitsonen, A. Smogunov, P. Umari and R. M. Wentzcovitch, *J. Phys.: Condens. Matter*, 2009, **21**, 395502.